Journal of Controlled Release 365 (2024) 358–368

Contents lists available at ScienceDirect

Journal of Controlled Release

journal homepage: www.elsevier.com/locate/jconrel

CCL2 chemokine inhibition primes the tumor vasculature for improved nanomedicine delivery and efficacy

Diana Möckel [a], Matthias Bartneck [b], Patricia Niemietz [c], Maike Wagner [a], Josef Ehling [a], Elena Rama [a], Marek Weiler [a], Felix Gremse [a,d], Dirk Eulberg [e], Robert Pola [f], Michal Pechar [f], Tomas Etrych [f], Gert Storm [g,h,i], Fabian Kiessling [j], Frank Tacke [c], Twan Lammers [a,*]

[a] Department of Nanomedicine and Theranostics, Institute for Experimental Molecular Imaging, RWTH Aachen University Clinic, Aachen, Germany
[b] Department of Medicine III, Medical Faculty, RWTH Aachen University Clinic, Aachen, Germany
[c] Department of Hepatology and Gastroenterology, Campus Virchow-Klinikum and Charité Campus Mitte, Charité - Universitätsmedizin Berlin, Germany
[d] Gremse-IT GmbH, Aachen, Germany
[e] TME Pharma AG, Berlin, Germany
[f] Czech Academy of Sciences, Institute of Macromolecular Chemistry, Prague, Czech Republic
[g] Department of Pharmaceutics, Utrecht University, the Netherlands
[h] Department of Biomaterials, Science and Technology, University of Twente, the Netherlands
[i] Department of Surgery, Yong Loo Lin School of Medicine, National University of Singapore, Singapore
[j] Institute for Experimental Molecular Imaging, RWTH Aachen University Clinic, Aachen, Germany

ARTICLE INFO

Keywords:
Chemokine signaling
CCL2
Tumor targeting
Nanomedicine
EPR
Imaging

ABSTRACT

Blood vessel functionality is crucial for efficient tumor-targeted drug delivery. Heterogeneous distribution and perfusion of angiogenic blood vessels contribute to suboptimal accumulation of (nano-) therapeutics in tumors and metastases. To attenuate pathological angiogenesis, an L-RNA aptamer inhibiting the C—C motif chemokine ligand 2 (CCL2) was administered to mice bearing orthotopic 4T1 triple-negative breast cancer tumors. The effect of CCL2 inhibition on tumor blood vessel functionality and tumor-targeted drug delivery was evaluated via multimodal and multiscale optical imaging, employing fluorophore-labeled polymeric (10 nm) and liposomal (100 nm) nanocarriers. Anti-CCL2 treatment induced a dose-dependent anti-angiogenic effect, reflected by a decreased relative blood volume, increased blood vessel maturity and functionality, and reduced macrophage infiltration, accompanied by a shift in the polarization of tumor-associated macrophages (TAM) towards a less M2-like and more M1-like phenotype. In line with this, CCL2 inhibitor treatment improved the delivery of polymers and liposomes to tumors, and enhanced the antitumor efficacy of free and liposomal doxorubicin. Together, these findings demonstrate that blocking the CCL2-CCR2 axis modulates TAM infiltration and polarization, resulting in vascular normalization and improved tumor-targeted drug delivery.

1. Introduction

Efficient delivery of drugs to and into solid tumors is one of the key challenges of systemic anticancer therapy. Various cell types in solid tumors produce growth factors, chemokines and cytokines, which induce angiogenesis, vascular remodeling and recruitment of myeloid and lymphoid cells [1]. This proangiogenic environment leads to leaky blood vessels with relatively poor blood flow [2]. Nanomedicine formulations, such as liposomes, polymers and micelles exploit this leaky vasculature for relatively site-specific accumulation in tumors, via the Enhanced Permeability and Retention (EPR) effect [3–7]. However, nanomedicine (and standard drug) delivery suffers from the poor and heterogeneous blood flow in tumors [8–11].

Tumor-associated macrophages (TAM) are important constituents of the tumor microenvironment and mediators of pathological angiogenesis [12–14]. TAM originate from monocytes produced in the bone marrow, and they are attracted from the bloodstream into tumors by inflammatory mediators. The latter include chemokines and cytokines, which are secreted by cancer cells and stromal cells [12,15]. The C—C motif chemokine ligand 2 (CCL2; also known as monocyte chemoattractant protein-1, MCP-1) is a potent chemoattractant which is widely expressed in various different tumor types [13,15,16]. Inflammatory

* Corresponding author.
E-mail address: tlammers@ukaachen.de (T. Lammers).

https://doi.org/10.1016/j.jconrel.2023.11.044
Received 21 December 2022; Received in revised form 20 October 2023; Accepted 22 November 2023
Available online 30 November 2023

monocytes express the C—C chemokine receptor (CCR2) and sense tumor-originating CCL2 chemokine gradients to promote monocyte infiltration and TAM tumor colonization [12,14,16]. Inhibition of CCL2-CCR2 signaling has been shown to block monocyte recruitment, attenuate pathological angiogenesis [14,17] and prolong the survival of tumor-bearing mice [18,19].

Considering that tumor blood vessels are heterogeneously distributed and only partially perfused, and that the resulting chaotic vascular network impairs efficient drug delivery to tumors, we set out to "normalize" [11] the tumor vasculature by blocking the infiltration of CCR2-positive pro-angiogenic macrophages. This was done via systemic subcutaneous treatment with an anti-CCL2 L-RNA aptamer. We employed the polyethylene glycol conjugated, anti-CCL2 mirror image oligonucleotide (Spiegelmer) mNOX-E36, a murine-specific analogue of NOX-E36 (also known as emapticap pegol), which has been tested in patients with type 2 diabetes mellitus and albuminuria [20]. mNOX-E36 binds and neutralizes mouse chemokine CCL2 at low nanomolar concentrations [21]. In mice with liver fibrosis, we previously showed that mNOX-E36 inhibits infiltrating macrophage-mediated pathological angiogenesis [14]. In a combined fibrosis-hepatocellular carcinoma (HCC) mouse model, we demonstrated that $CCR2^{+}$ macrophages are primarily present in the highly vascularized tumor rim, that they have a distinct pro-angiogenic expression profile, and that mNOX-E36 attenuates pathogenic vascularization and tumor volume [17].

In this study, we explored the potential of mNOX-E36-mediated CCL2 inhibition (CCL2i) to normalize the tumor vasculature in a mouse model of triple-negative breast cancer (TNBC). TNBC is one of the most difficult to treat breast cancers, and is characterized by a highly angiogenic and poorly perfused vascular network [22–24]. To investigate the effect of CCL2i on TNBC vascularization and tumor-directed drug delivery, two different doses of mNOX-E36 (5 and 20 mg/kg) were s.c. administered 3 times per week for 2 weeks, to Balb/cAnNRj mice bearing syngeneic and orthotopically inoculated 4T1 TNBC tumors (Fig. 1). Upon extensive characterization of the tumor vasculature and microenvironment, we visualized and quantified the tumor accumulation and intratumoral distribution of fluorophore-labeled poly (N-(2-hydroxypropyl)methacrylamide) polymers (PHPMA; 10 nm; labeled with Dy750 and Atto488), pegylated liposomes (100 nm; labeled with Cy7 and BDP-FL) and a free fluorophore (1 nm; Cy7; serving as a small molecule model drug). Near-infrared fluorophores were used for in vivo CT-FMT imaging up to 72 h after i.v. administration. Standard fluorophores were used for ex vivo fluorescence microscopy, two-photon laser scanning microscopy and flow cytometry. We finally combined mNOX-E36 with free doxorubicin and doxorubicin-loaded liposomes, to assess the added value of CCL2i -induced vascular priming on anticancer treatment outcome (Fig. 1).

2. Materials and methods

2.1. Diagnostic agents

CT-based vascular in vivo imaging was done using an iodine-based radiopaque blood pool contrast agent (eXIA 160XL, binitio Biomedical Inc., Ottawa, Canada). eXIA was intravenously injected into the lateral tail vein at a dose of 0.1 ml per 20 g body weight (BW). At the end of the imaging experiment, mice were intracardially perfused with Microfil (Flow Tech, Carver, MA, USA), a polymerizing lead-containing silicone rubber contrast agent for high-resolution 3D CT investigation of the tumor blood vessel microarchitecture. The NIR fluorophore Cy7 sizing about 1 nm (Lumiprobe GmbH, Hannover, Germany) was used as a small molecule model drug for biodistribution assessment and for imaging of tumor targeting. Double fluorophore-labeled PHPMA polymers (10 nm) [25] and pegylated liposomes (100 nm) [26] were used as nanocarriers (see below for details). Free dye, polymers and liposomes were injected intravenously at the dosages of 2 nmol dye in 50 µl 0.9% sodium chloride solution.

2.2. PHPMA polymers

Polymers were synthesized as reported earlier in detail [27]. Briefly,

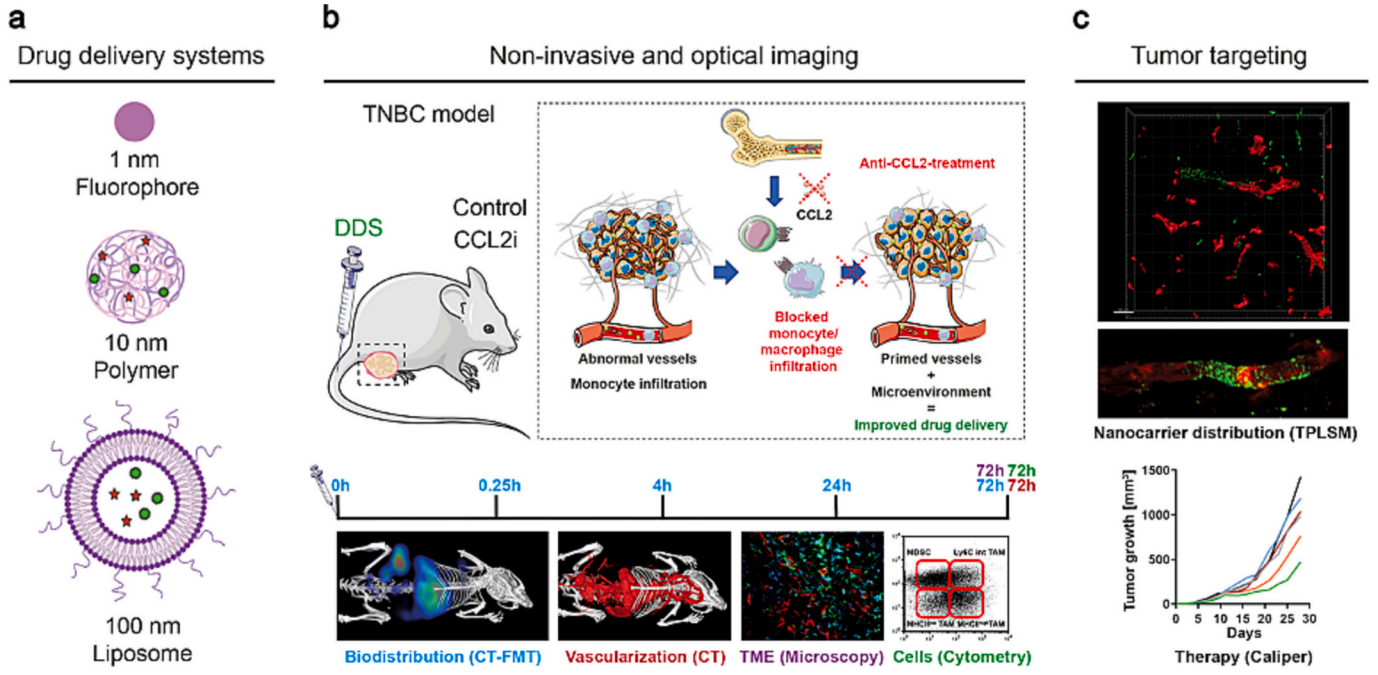

Fig. 1. Study design. We evaluated the effect of L-RNA aptamer-mediated CCL2 inhibition (CCL2i) on the tumor vasculature, tumor microenvironment and tumor-targeted drug delivery. (a) For the latter, free fluorophores and fluorophore-labeled polymeric and liposomal drug delivery systems (DDS) were employed. (b) The tumor accumulation and intratumoral distribution of model drugs and DDS, as well as the composition of the tumor microenvironment, were evaluated using CT-FMT, CT, fluorescence microscopy, two-photon microscopy, and flow cytometry. (c) L-RNA aptamer-mediated CCL2i was also combined with free and liposomal doxorubicin, to evaluate the potential of interfering with CCL2 signaling on therapeutic outcome.

radical copolymerization of *N*-(2-hydroxypropyl) methacrylamide (HPMA; 85 mol%) and 3-(*N*-methacryloyl glycylglycyl)thiazolidine-2-thione (Ma-GG-TT; 15 mol%) were done in DMSO at 50 °C for 6 h yielding the copolymer precursor poly(HPMA-*co*-Ma-GG-TT). The fluorophores Atto 488-NH_2 and Dy750-NH_2 were added to the solution of the polymer precursor (10% *w*/w) in *N,N*-dimethylacetamide, and *N,N*′-diisopropylethylamine (equimolar amount related to the fluorophores) was added. The remaining TT groups of the polymer were aminolyzed with 1-aminopropan-2-ol and the labeled polymer was precipitated with diethylether. The product was purified using gel filtration on PD-10 desalting columns containing Sephadex G-25 resins in water. Size-exclusion chromatography equipped with refractive index and multi-angle light scattering detectors revealed a hydrodynamic radius of 4.1 nm and a polydispersity index of 1.7 for the 67 kDa pHPMA polymer. In physiologically relevant solutions, e.g. in blood plasma, the size of these coiled-coil polymers was determined to be 10–20 nm via fluorescence correlation spectroscopy [25]. Dye contents were 2.1%*w*/w for Atto488 and 1.6%w/w for Dy750, as assessed by UV/VIS spectrophotometry.

2.3. Pegylated liposomes

Liposomes were based on the clinically used lipids dipalmitoylphosphatidylcholine (DPPC), cholesterol, and 1,2-distearoyl-sn-glycero-3-phosphoethanolamine-N-[methoxy-(polyethylene glycol)-2000] (DSPE-PEG). Liposomes were fluorescently labeled with Cy7-NHS-ester or BDP-FL (Lumiprobe GmbH, Hannover, Germany) bound to 1,2-distearoyl-sn-glycero-3-phosphorylethanolamine (DSPE) via NHS-amine reaction. Lipids were mixed in a flask, dissolved in $CHCl_3$, dried on a rotary evaporator and rehydrated with PBS applying the thin film method [28] at 70 °C. After 2 h of rehydration, the liposome mixture was extruded using a Liposofast LF-50 extruder (Avestin, Ottawa, Canada) at 70 °C. The filter pore sizes which were used for extrusion were 200 nm and 100 nm. After extrusion a liposome size of approx. 100 nm was obtained, with a polydispersity index <0.1. Dye content was measured with a well-plate fluorimeter (M200 pro, Tecan AG, Switzerland) using the free dye as a standard.

2.4. Therapeutic agents

The CCL2-inhibiting L-RNA aptamer mNOX-E36 (50-nucleotide L-RNA oligonucleotide; 5′-GCGACAUUGGUUGGGCAUGAGGCGAGGCCC UUUGAUGAAUCCGC-GGCCA-3′), conjugated at the 3′ end with 40 kDa PEG was provided by TME Pharma AG (Berlin, Germany). mNOX-E36-based CCL2i therapy was subcutaneously injected 3 times per week at 5 and 20 mg/kg in 100 µl 5% glucose solution, in the neck region of the mice. 5% glucose solution was used as the vehicle control. For the chemotherapy study, only the 20 mg/kg dose was used for CCL2i. Chemotherapy started 5 days after the anti-CCL2 treatment with the following 8 groups: control, control + CCL2i (20 mg/kg), doxorubicin (5 mg/kg), doxorubicin + CCL2i, liposomal Dox (Doxil; 5 mg/kg), and liposomal Dox + CCL2i.

2.5. Animal model

All animal experiments were approved by the German State Office for Nature, Environment and Consumer Protection (LANUV) North Rhine-Westphalia. In total, 75 BALB/cAnNRj mice (female; age 10–12 weeks; Janvier Labs, Saint Berthevin, France) were housed in groups of five animals under specific pathogen free conditions with a 12 h light/dark cycle. The environment was temperature (20–24 °C) and humidity (45–65%) controlled according to the guidelines of the "Federation for Laboratory Animal Science Associations" (FELASA, www.felasa.eu). Acidified water and standard pellets for laboratory mice (ssniff GmbH, Soest, Germany) were offered ad libitum.

4T1 murine triple-negative breast cancer cells (American Type Culture Collection, Manassas, VA, USA) were cultured in RPMI medium (RPMI 1640; Gibco, Life Technologies GmbH, Germany), supplemented with 10% fetal bovine serum (FBS; Life Technologies GmbH, Germany) and 1% penicillin/streptomycin (10,000 U/ml penicillin; 10 mg/ml streptomycin, Life Technologies GmbH, Germany) at 37 °C and 5% CO_2 in a humid atmosphere.

Mice were orthotopically inoculated with 2.5 x 10E4 4T1 TNBC cells into the right abdominal mammary gland. Tumor growth was monitored daily via caliper measurement and for the chemotherapy study also via µCT at the beginning and end of the therapy. Tumors were grown until the end of the experiment or until the termination criteria according to the score sheet have been reached. As soon as the tumors were palpable, the mice were randomly divided into groups (with 5 mice per group) and anti-CCL2 treatment was initiated.

For the study with the fluorescent model drugs and delivery systems, mice were fed with chlorophyll-free food (ssniff GmbH, Soest, Germany) to minimize autofluorescence in fluorescence-mediated tomography. The fur of the animals was removed before starting the fluorescence measurements, since hair leads to a dispersion of the fluorescence signal and thus prevents an exact localization of the signal.

Anesthesia was induced by 4% isoflurane (Forene, Abbott, Wiesbaden, Germany) in oxygen-enriched air using a vaporizer. During injections and imaging, the isoflurane concentration was reduced to 2.0% and eyes were kept hydrated with Bepanthen eye ointment (Bayer Vital GmbH, Germany). All i.v. treatments were injected into the lateral tail vein of the mice using a catheter constituted by a 30 G cannula (B. Braun, Melsungen, Germany) and a polyethylene tube (Hartenstein, Würzburg, Germany).

2.6. In vivo imaging

Before and after injection of the drug delivery systems (DDS), mice were positioned in a micro-computed tomography (µCT) - fluorescence-mediated tomography (FMT) compatible mouse bed. Imaging was performed before and 4, 24 and 72 h after i.v. injection. Mice were first scanned using a dual energy flat-panel µCT scanner (TomoScope 30s Duo, CT-Imaging, Erlangen, Germany), acquiring 720 projections containing 1032 × 1012 pixels in 1.1 full rotations within 90 s, upon which the volumetric data sets were reconstructed at an isotropic voxel size of 35 µm using a Feldkamp type algorithm and a smooth kernel. Subsequently, the mouse bed was transferred to the FMT (FMT 2500 LX, PerkinElmer, MA, USA), and FMT scans were performed at 750 nm using 115–120 grid points. To avoid unspecific signals from stomach, intestine or bladder in the FMT, the mice were fed with chlorophyll-free food.

At 72 h, tumor-bearing mice were also scanned before and after the i.v. injection (100 µl) of an iodine-based blood-pool radiopaque contrast agent (eXIA 160XL, binitio Biomedical Inc., Ottawa, Canada) optimized for in vivo µCT, acquiring 2880 projections over a 6-min time frame. Tumors were three-dimensionally segmented using Imalytics Preclinical (Gremse-IT, Aachen, Germany) [29] and the relative blood volume (rBV) was determined.

The µCT-FMT scanning, reconstruction and image analysis were performed as described in [30]. The 3D image data were analyzed using interactive image analysis software [30]. Absorption and scatterings maps, which are important for quantitative fluorescence reconstruction, were derived using the µCT data [31]. The combination of FMT and µCT allows for a more user-independent analysis because the organs can be delineated based on the µCT data [32]. Tumors and organs were manually pre-segmented, by delineating the tumor margins in all three axes in the CT images. After this segmentation, the corresponding FMT data set was loaded as an image overlay, and the software computed the volume and fluorescence concentration for each segmented region. This information was used to determine the percentage of the injected dose per gram (%ID/g) accumulating in tumors.

2.7. Ex vivo imaging

After the last in vivo scan, rhodamine-lectin (*Ricinus Communis* Agglutinin I Rhodamine, Vector Laboratories, CA, USA) was administered i.v. for later immunohistochemistry to identify functional vessels. Fifteen min after rhodamine-lectin injection, animals were sacrificed and tumors and organs were harvested, weighed and analyzed by 2D FRI (Fluorescence Reflectance Imaging).

One mouse per group was intracardially perfused with Microfil (Flow Tech, Carver, MA, USA), i.e. a lead-containing silicone rubber CT contrast agent for high-resolution 3D investigation of the microarchitecture of blood vessels in the tumor, which polymerizes within the vascular compartment. Perfusion was performed by direct infusion of 20 ml PBS for complete blood removal, 20 ml 4% paraformaldehyde for vessels fixation and 5 ml Microfil (MV-112, MV-Diluent and curing agent; Flow Tech, Carver, MA) into the left ventricle (after incising the inferior vena cava) at physiological pressures, using a perfusion pump (PHD 2000 Infusion; Harvard Apparatus, Holliston, US) as described in [33]. After Microfil perfusion and formalin-fixation, tumors were excised, formalin-fixed and scanned using a SkyScan 1272 μCT system (SkyScan, Kontich, Belgium). Tumors were positioned on a computer-controlled rotation platform and scanned 180° around the vertical axis, in rotation steps of 0.3° at 60 kV. Acquisition times ranged from 2 to 4 h. The generated pixel sizes ranged from 3.4 to 5.3 μm. 3D volume rendering of reconstructed high-resolution μCT data sets was performed with Imalytics Preclinical (Gremse-IT, Aachen, Germany).

2.8. Immunohistochemistry

Tumors and organs were embedded in Tissue-Tek (Sakura Finetek Germany GmbH, Staufen, Germany) and stored at −80 °C. Eight μm thick cryosections were prepared with a rotary microtome (Leica CM3050 S, Leica, Wetzlar, Germany) and stored at −80 °C.

Immunofluorescence analysis was done using the following antibodies: rat anti-mouse CD31 antibody (BD Biosciences, Heidelberg, Germany) for staining endothelial cells; rat anti-mouse F4/80 antibody (AbD Serotec, Puchheim, Germany) for macrophages; rat anti-mouse CD206/MRC1 antibody (Origene, Herford, Germany) to detect M2-like macrophages; a biotinylated antibody against α-smooth muscle actin (Progen, Heidelberg, Germany) was used to visualize mature vessels. Secondary antibodies were obtained from Dianova (Hamburg, Germany). 4′,6-diamidino-2-phenylindole (DAPI) (Merck, Germany) was used for nuclei counterstaining, and sections were mounted using Mowiol.

The staining protocol entailed fixation for 5 min with 80% MeOH / 100% acetone, primary antibodies incubation, triplicate washing, secondary antibody staining, triplicate washing, and finally embedding with Mowiol 4–88 (Sigma-Aldrich, Taufkirchen, Germany). Fluorescence microscopy was performed using an Axio Imager M2 microscope (Carl Zeiss Microscopy GmbH, Germany) and a high-resolution camera (AxioCam MRm Rev.3, Carl Zeiss Microscopy GmbH, Germany).

For quantification of tumor blood vessels, mature vessels, functional vessels and macrophages, six micrographs (100× magnification) from three representative sections per tumor and five different tumors per group were analyzed and averaged. Area fractions of rhodamine-lectin (functional blood vessels), F4/80-positive macrophages, CD31-positive vessels and SMA-positive vessels were determined. Quantifications were performed using the AxioVision Rel 4.9 software (Carl Zeiss Microscopy GmbH, Germany).

Representative tumor samples were obtained from formalin-fixed, paraffin-embedded (FFPE) tissue blocks. Five μm thick tissue sections were taken to perform the H&E stainings. H&*E*-stained slides were scanned using the PerkinElmer Vectra 3.0 automated quantitative pathology imaging system. Whole-section slide images (at 100× magnification) were evaluated and three areas were randomly selected. The percentage area fractions of cancer cells, stromal cells and lymphocytes were analyzed (at 200× magnification) and the averages of 5 selected areas were calculated and compared.

2.9. Two-photon laser scanning microscopy (TPLSM)

Cryosections of 4T1 tumors with a slice thickness of 100 μm were prepared with a rotary microtome (Leica CM3050 S, Leica, Wetzlar, Germany). Tumor slices were imaged using an Olympus FV1000MPE multiphoton microscopy system (Mai Tai DeepSee pulsed Ti:Sapphire laser with 140 fps pulse width at an excitation wavelength of 800 nm and a 25× water-immersed objective (NA [numerical apertures] = 1.05, WD [working distance] = 2 mm). Three internal photon multiplier tubes were used to detect the fluorescence signals, and filters were adjusted to the corresponding spectra: 390 to 460 for collagen second harmonic imaging (Col-I and Col-III), 490 to 540 for the green fluorescence of liposomes and polymers, and 590 to 620 for rhodamine-lectin. TPLSM images were analyzed using Image-Pro Analyzer 7.0 software (Media Cybernetis, Inc) and Imaris 7.4 (Bitplane AG, Switzerland) [34]. For the micro-distribution analysis of polymers and liposomes, an adapted version of the “dilate surface” Xtension in Imaris was applied [25,26].

2.10. Flow cytometry and fluorescence-activated cell sorting

Tumor-bearing mice were intracardially perfused with 20 ml PBS for complete blood removal by direct infusion into the left ventricle at physiological pressure, using a perfusion pump. After perfusion, tumors were excised and kept on ice. Suspensions of single leukocytes were obtained by mincing tumor tissue into pieces of <1 mm. Collagenase digestion was done for 30 min using type IV collagenase (Worthington, NJ, USA). Blood was subjected to red blood cell lysis using Pharm Lyse (Becton Dickinson, NJ, USA). Cells were stained with CD45, CD11b, Ly6G, Gr1, F4/80, and MHCII (all BD Biosciences, NJ, USA). For staining T lymphocytes, staining was performed using a combination of CD45, TCRβ and CD8a antibodies (BD Biosciences, NJ, USA).

To gain maximum purity of cell populations for cell sorting of myeloid tumor leukocytes, cell suspensions were pre-purified for cell sorting using CD11b enrichment using magnetic-assisted cell sorting (Miltenyi Biotec, Bergisch-Gladbach, Germany). In addition, lineage staining of lymphoid cells (CD4, CD8, B220, and NK1.1; all BD Biosciences, NJ, USA) was done to remove lymphocytes. For a detailed protocol see [17]. Analysis was performed using a FACS Fortessa and a BD FACS Aria II SORP Cell Sorter (both BD Biosciences, Franklin Lakes, NJ, USA) was used for cell sorting. Flow cytometric data were analyzed using FlowLogic (Miltenyi Biotec, Bergisch-Gladbach, Germany).

2.11. Statistical analysis

Data are presented as mean ± standard deviation (SD). All data were tested for normal distribution with the Shapiro-Wilk normality test. The two-tailed unpaired Student's *t*-test was applied for comparison between two groups. One-way analysis of variance (ANOVA) followed by Bonferroni post-hoc testing was employed for more than two groups. Statistical analysis was performed using GraphPad Prism 9.1 (San Diego, CA, USA). *P*-values <0.05 were considered significant.

3. Results and discussion

3.1. CCL2 inhibition induces vascular normalization

BALB/c mice bearing orthotopic 4T1 tumors were treated with 5 and 20 mg/kg of the anti-CCL2-inhibiting RNA aptamer mNOX-E36 once tumors were palpable (2–3 mm in diameter). The RNA aptamer was s.c. administered 3 times weekly for 2 weeks. The vascular effects of CCL2 inhibitor (CCL2i) therapy were evaluated using in vivo contrast-enhanced micro-computed tomography (μCT), ex vivo high-resolution μCT, and immunofluorescence microscopy. CT imaging showed a

reduction in the relative blood volume (rBV) in tumors upon CCL2i treatment (Fig. 2a). High-resolution ex vivo μCT confirmed this notion, showing a smaller tumor size and decreased vascular density (Fig. 2b). Immunohistochemistry and immunofluorescence microscopy analysis of CD31$^+$ (all blood vessels; blue), RCA-I-lectin$^+$ (perfused blood vessels; red) and αSMA$^+$ (mature blood vessels; green) are in line with this, illustrating a reduction in rBV paralleled by a higher fraction of perfused and more mature blood vessels (Fig. 2c-d). Blood vessel formation was

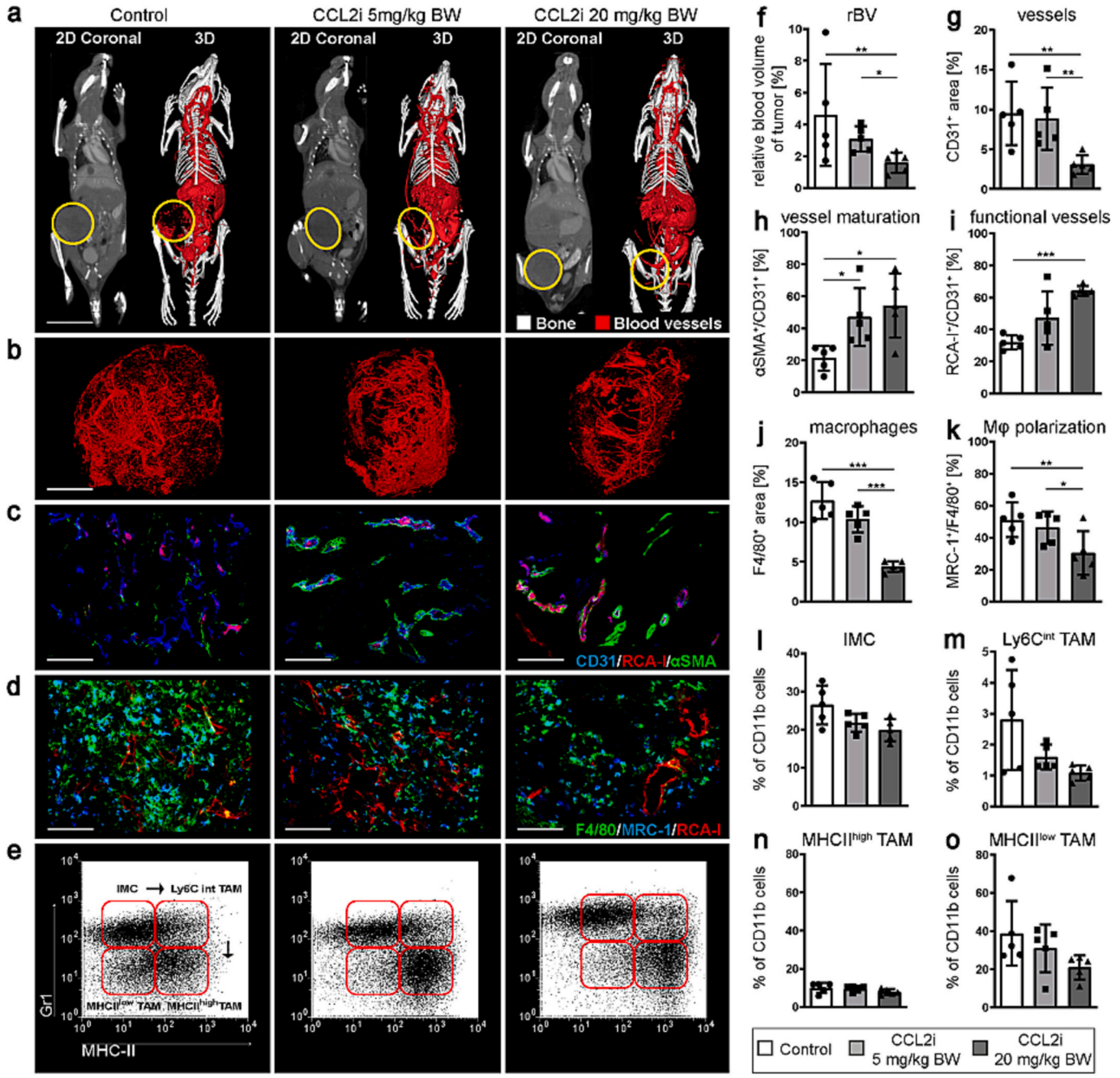

Fig. 2. CCL2 inhibition induces vascular normalization and macrophage polarization. (a) Visualization of tumor blood vessels via in vivo μCT using an iodine-based blood contrast agent (eXIA 160XL), indicating a reduction in the relative blood volume (rBV) in tumors upon treatment with 5 or 20 mg/kg BW of the CCL2 inhibitor (CCL2i) mNOX-E36. Scale bar = 10 mm. (b) High-resolution ex vivo μCT imaging upon cardiac perfusion with the vascular casting agent Microfil enables a detailed 3D depiction of the microvascular architecture of excised tumors. Scale bar = 3 mm. Tumor size and vascular density are decreased upon CCL2i, in a dose-dependent manner. For full tumor growth curve, see Fig. 4A. (c) Immunofluorescence-based analysis of CD31$^+$ cells (all blood vessels; blue), RCA-I-lectin$^+$ (functional blood vessels; red) and αSMA$^+$ (mature blood vessels; green), illustrating a reduction in rBV paralleled by more perfused and more mature blood vessels. Scale bar = 100 μm. (d) Immunohistochemistry and immunofluorescence microscopy of F4/80$^+$ (all macrophages, green), MRC-1$^+$ (M2-like macrophages, blue) and RCA-I-lectin$^+$ (functional blood vessels, red), exemplifying a reduced tumor-associated macrophage (TAM) density and less M2-like TAM upon CCL2 inhibitor therapy. Scale bar = 100 μm. (e) Representative flow cytometry plots of tumor-associated myeloid cell populations (30,000 events shown, pre-gated on CD11b$^+$). (f) Quantification of relative blood volume (rBV), (g) blood vessels, (h) mature blood vessels, (i) functional blood vessels, (j) macrophages, (k) M2-like macrophages in IHC, and (l) IMC = immature myeloid cells, (m) Ly6C^{int} TAM, (n) MHC^{high} TAM = pro-inflammatory M1-like macrophages and (o) MHC^{low} TAM = pro-tumorigenic M2-like macrophages in FACS upon CCL2 inhibitor treatment. Bars represent mean ± SD of $n = 5$ data points (tumors) per group; $^*p < 0.05$, $^{**}p < 0.01$, $^{***}p < 0.001$. (For interpretation of the references to colour in this figure legend, the reader is referred to the web version of this article.)

most prominently reduced at the 20 mg/kg dose of CCL2i (Fig. 2f-g). Concurrently, the fraction of mature and perfused vessels was highest for this highest dose (Fig. 2h-i).

In agreement with our hypothesis, we noted a dose-dependent reduction of F4/80^{+} tumor-associated macrophages (TAM) upon CCL2i (Fig. 2d,j). To connect the angiogenesis-suppressing effects of CCL2 inhibition to specific TAM populations, the tumor myeloid immune cell composition was analyzed. Immunofluorescence microscopy was done based on the pan-macrophage marker F4/80 and the mannose receptor C-type 1 (MRC-1; CD206; which identifies pro-tumorigenic M2-like macrophages). Immunohistochemistry demonstrated that total F4/80^{+} cells and F4/80^{+}/MRC-1^{+} double-positive cells were both reduced upon CCL2i treatment (Fig. 2d,j,k), pointing towards an altered TAM polarization, with a particular reduction of alternatively activated M2-like phagocytes. In line with this, flow cytometry showed a decrease in CD11b^{+} monocyte-derived macrophages in tumors upon CCL2i, with a dose-dependent reduction particularly obvious for Gr1^{low}MHCII^{low} M2-like TAM, and not for Gr1^{low}MHCII^{high} M1-like TAM (Fig. 2e, l-o). These TAM populations exert various functions with regard to modulating tumorigenesis, tumor progression, immune suppression and vascularization (including response to hypoxia and production of angiogenic factors such as VEGF-A), and they are also an important source of matrix metalloproteinases (MMP) which mediate ECM degradation [35–39]. We hypothesize that CCL2i-based pharmacological modulation of TAM populations in tumors may contribute to induction of vessel normalization and improvement of tumor blood flow and tumor-targeted drug delivery.

3.2. CCL2 inhibition improves nanomedicine tumor accumulation and penetration

To visualize and quantify the tumor accumulation of nanocarrier materials after 6 administrations of CCL2i therapy, 4T1 tumor-bearing mice were injected with a near-infrared free dye and with

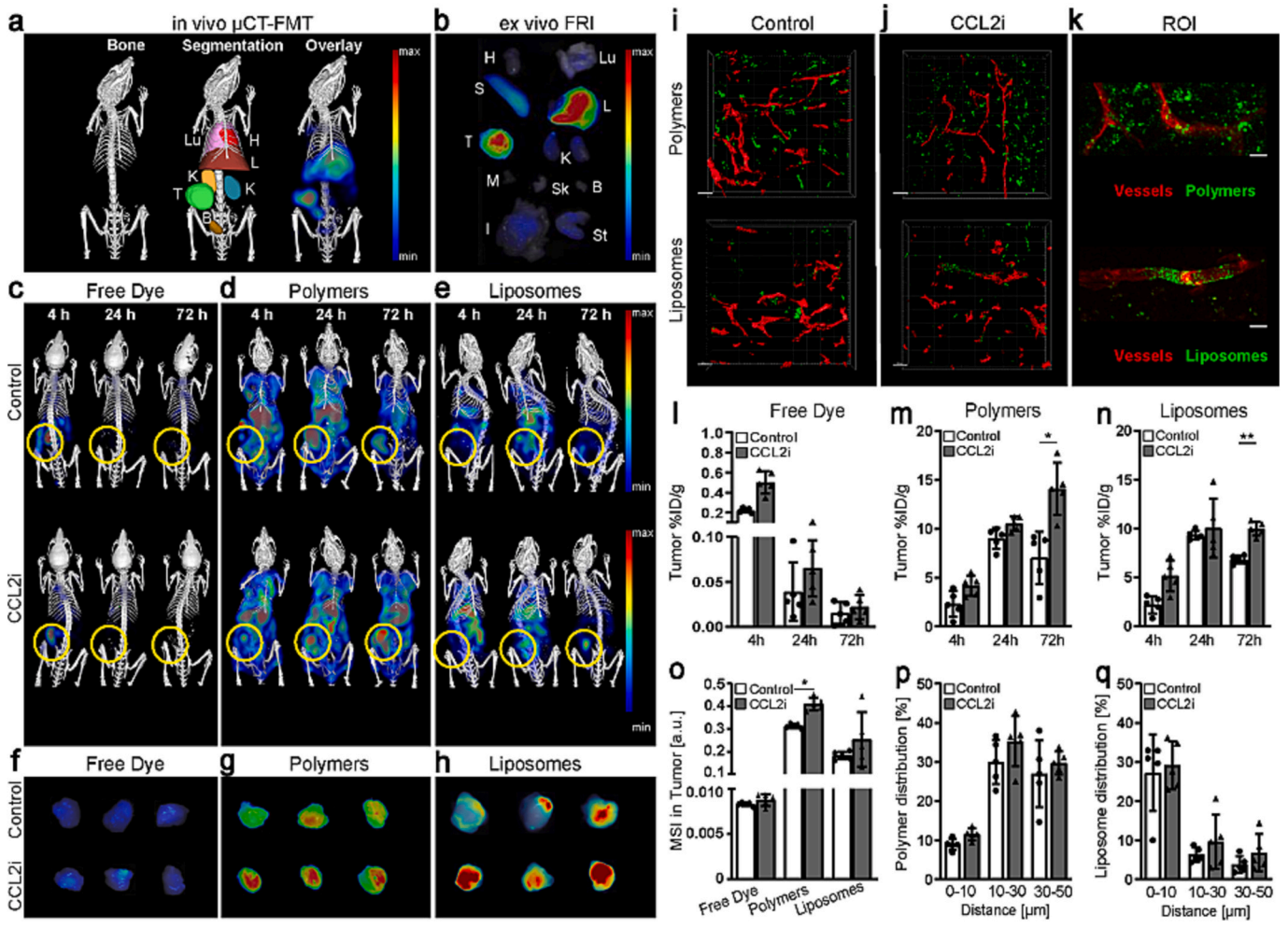

Fig. 3. CCL2 inhibition improves nanomedicine tumor targeting. (a) Representative 3D CT-based tissue segmentation (H = Heart; Lu = Lungs; L = Liver; K = Kidneys B = Bladder; T = Tumor) and FMT signals of liposome accumulation at 72 h post i.v. injection upon CCL2i therapy. (b) Example of 2D FRI images of liposome accumulation at 72 h post i.v. injection upon CCL2i therapy (abbreviations as above, plus: S = Spleen; M = Muscle; Sk = Skin; I = Intestine; St = Stomach). (c-e) Representative images for non-invasive CT-FMT imaging of the whole mouse for (c) free dye, (d) polymers and (e) liposomes over time for control and CCL2i treated mice (yellow circle = tumor). (f-h) Representative ex vivo FRI scans for tumor accumulation in control and CCL2i groups for (f) free dye, (g) polymers and (h) liposomes at 72 h p.i. (i-k) Two-photon laser scanning microscopy analysis of polymer and liposome penetration and distribution in (i) control tumors and (j) upon CCL2i treatment, with a 3D reconstructed region of interest in (k). (l-n) Quantification of the tumor accumulation, in percent of the injected dose per gram tumor tissue (%ID/g), at 4, 24 and 72 h post i.v. injection of (l) free dye, (m) polymers and (n) liposomes upon control and CCL2i treatment. Data are mean ± SD of $n = 5$ per group. (o) Mean ex vivo FRI signal intensity in tumors at 72 h p.i. (p-q) Quantification of the tumor penetration of (p) polymeric and (q) liposomal nanocarriers. Plotted are the relative amounts of nanocarriers in three compartments at different distances from the vessel surface. Bars are mean ± SD of $n = 6$ micrographs from $n = 3$ representative sections per tumor, for n = 5 tumors per group. Each data point represents an individual tumor. Scale bar = 50 µm (i,j) and 200 µm (k). *$p <$ 0.05, **$p < 0.01$. (For interpretation of the references to colour in this figure legend, the reader is referred to the web version of this article.)

fluorescently double-labeled 10 nm PHPMA polymers and 100 nm pegylated liposomes. Due to the dose-dependency of the observed vascular priming, we only used 20 mg/kg mNOX-E36 for these examinations. Scans were performed before and 4, 24 and 72 h after i.v. injection of the free dye and dye-labeled nanocarriers. Upon reconstruction of the μCT-FMT data and segmentation of the tissues, the nanocarriers' fluorescence signals were fused using Imalytics Preclinical software (Fig. 3a-b) [29]. For quantification, calibration factors were determined using phantoms loaded with fixed amounts of fluorophores, enabling calculation of the percentage of the injected dose per gram (% ID/g) tumor tissue.

Representative images of the biodistribution and tumor accumulation of free dye, polymers and liposomes with and without anti-CCL2 treatment are shown in Fig. 3c-h. The images show very fast elimination of free Cy7 (whose biodistribution is influenced by interactions with plasma proteins and organic anion transporting polypeptides [40,41]), with barely detectable levels of tumor accumulation beyond the 4 h time point, regardless of CCL2i (Fig. 3c,f). Polymers and liposomes remained detectable for much longer periods of time and showed much higher levels of tumor accumulation (Fig. 3d,e,g,h).

Quantification of free dye, polymer and liposome tumor accumulation is presented in Fig. 3l-n. For the 1 nm model drug, tumor concentrations increased from 0.2 to 0.5 %ID/g upon anti-CCL2 treatment at 4 h post injection, but this difference was not significant ($p = 0.08$; Fig. 3c, l). For 10 nm PHPMA polymer, CCL2i treatment increased the levels localizing to tumors at 72 h p.i. from 6.9 to 14.1 %ID/g ($p = 0.03$; Fig. 3d,m). For 100 nm pegylated liposomes, tumor accumulation also significantly increased upon CCL2i, from 6.8 to 10.1 %ID/g ($p = 0.006$; Fig. 3e,n). These in vivo findings were confirmed by means of ex vivo FRI (Fig. 3f-h,o).

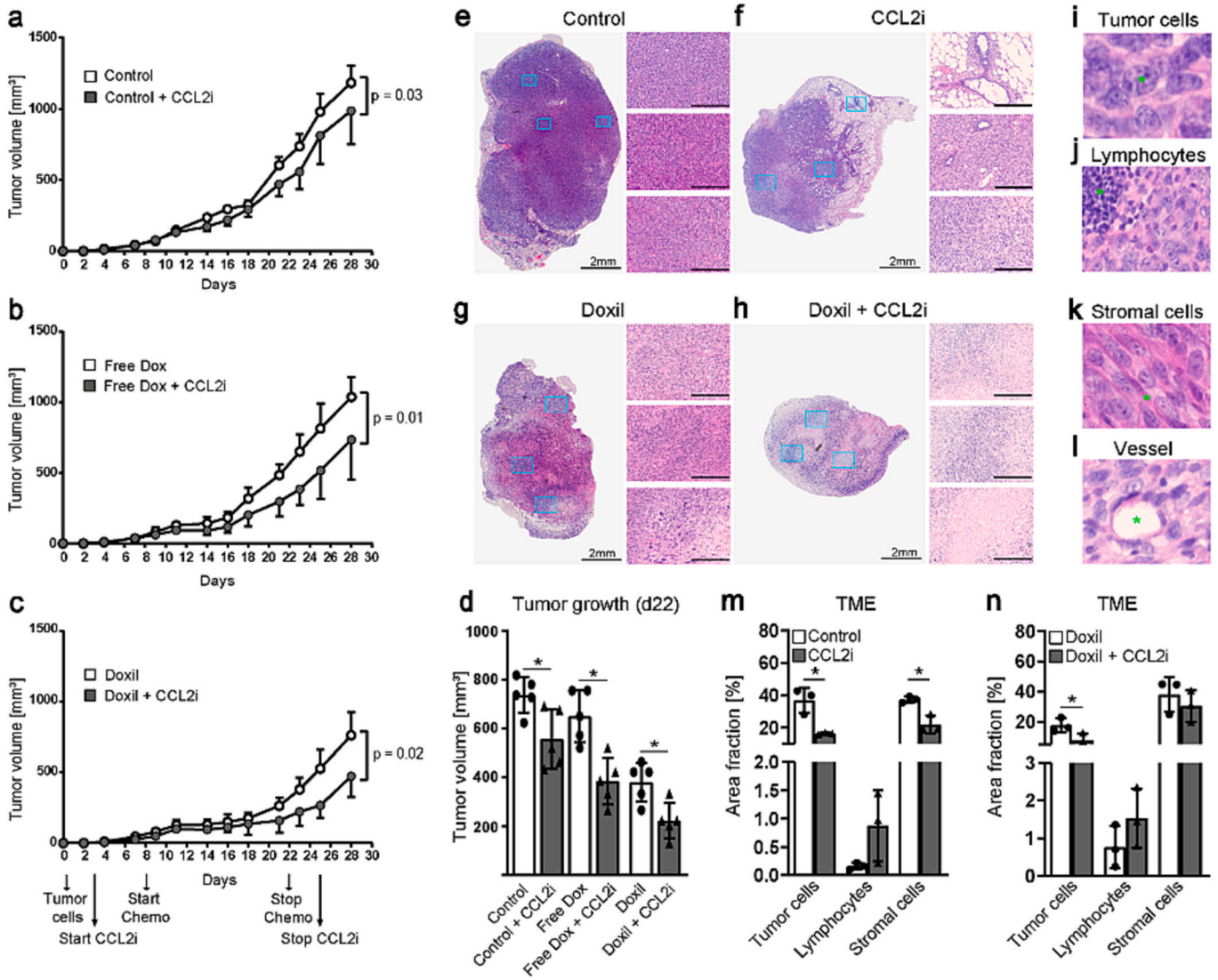

Fig. 4. CCL2 inhibition enhances (nano)chemotherapy antitumor efficacy and modulates the composition of the tumor microenvironment. (a-c) Growth inhibition of orthotopic 4T1 tumors upon treatment with (a) Control vs. Control + CCL2i, (b) Free Dox vs. Free Dox + CCL2i, and (c) Doxil vs. Doxil + CCL2i. (d) CCL2 inhibition significantly enhances antitumor responses, as exemplified by head-to-head comparison at the last day of (nano)chemotherapy administration. (e-h) H&*E*-stained whole tumor sections and selected regions of interest for (e) Control, (f) Control + CCL2i, (g) Doxil and (h) Doxil + CCL2i. Cells were classified into three cell classes based on nuclear morphology, i.e. (i) epithelioid cancer cells, (j) round tumor-infiltrating lymphocytes and (k) spindle-like stromal cells. (l) Identification of blood vessels in H&E staining tumor sections. (m-n) Quantification of tumor microenvironment composition assessing area fraction of tumor cells, lymphocytes and stromal cells for (m) Control vs. Control + CCL2i, and for (n) Doxil vs. Doxil + CCL2i. Scale bars overview images: 2 mm. Scale bar in zoom images = 100 μm. Data is presented shown as mean ± SD of $n = 5$ tumors per group for the growth inhibition study in panels a-c. Tumor volumes at day 22 are displayed for all n = 5 individual tumors. Area fraction values in panels m and n represent mean ± SD of $n = 6$ micrographs from $n = 3$ representative sections per tumor, for n = 3 tumors (data points) per group. *$p < 0.05$.

The enhanced tumor accumulation of polymers and liposomes correlated with histologically observed induction of vascular normalization (Fig. 2). From the literature, it is known that vascular normalization (which is typically induced using intermediately dosed anti-VEGFR2 or anti-VEGF treatment) can lead to increased accumulation of drugs and drug delivery systems in tumors, an effect that is mainly mediated by improved vascular organization and increased tumor perfusion [42–44].

To quantify the levels of nanocarrier penetration out of the blood vessels deep into the tumor interstitium, TPLSM imaging was performed in 100 μm-thick sections from tumors upon control vs. anti-CCL2 treatment (Fig. 3i-k). The highest amounts of 10 nm PHPMA polymers were found in compartments 10–50 μm away from the endothelial lining, while 100 nm liposomes mostly accumulated in the perivascular region, i.e. 0–10 μm from the tumor blood vessel wall (Fig. 3p,q). Distribution analysis indicated that particularly liposome penetration was enhanced by CCL2i, although the results were not statistically significant (Fig. 3p,q).

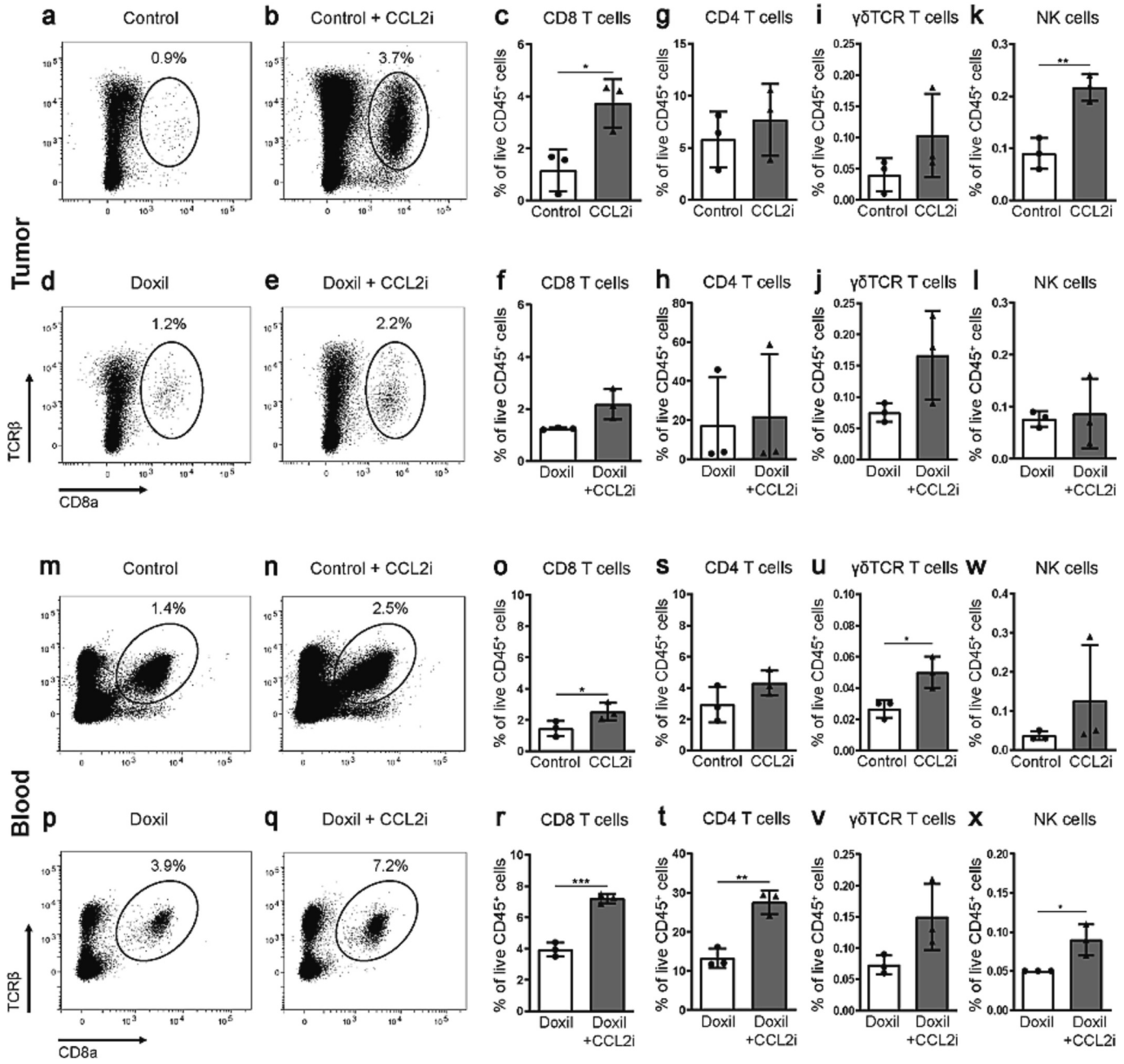

Fig. 5. Flow cytometry analysis of T and NK lymphocytes in tumor tissue and blood upon CCL2 inhibition and Doxil therapy. (a-f) Representative FACS plots and analyses of $CD8^+$ cytotoxic T cell infiltration in tumors, identified as $CD8a^+$ $TCR\beta^+$ double-positive cells for Control vs. Control + CCL2i (a-c) and for Doxil vs. Doxil + CCL2i (d-f). Analysis of $CD4^+$ T helper cells (g-h), $\gamma\delta TCR^+$ T cells (i-j) and NK cells (k-l) in tumor tissue for Control vs. Control + CCL2i and Doxil vs. Doxil + CCL2i. (m-x) FACS plots for $CD8^+$ T cells (m,n,p,q) and flow cytometry analysis of $CD8^+$ T cells (o,r), $CD4^+$ T cells (s-t), $\gamma\delta TCR^+$ Tcells (u-v) and NK cells (w-x) in blood for Control vs. Control + CCL2i and Doxil vs. Doxil + CCL2i treatment. Quantifications in both tumors and blood indicate increased levels of T and NK lymphocytes upon inhibition of CCL2. Bars represent mean ± SD of n = 3 tumors (data points) per group. $*p < 0.05$, $**p < 0.01$, $***p < 0.001$.

3.3. CCL2 inhibition improves the antitumor efficacy of free and liposomal doxorubicin

To evaluate the impact of CCL2 inhibition on the outcome of (nano) drug therapy, we applied free doxorubicin (Free Dox) and pegylated liposomal doxorubicin (Doxil) intravenously to 4T1 tumor-bearing mice co-treated with mNOX-E36. Tumor growth was studied over 4 weeks for 6 different groups: Control vs. Control + CCL2i; Free Dox vs. Free Dox + CCL2i; and Doxil vs. Doxil + CCL2i (Fig. 4a-c). Anti-CCL2 treatment significantly enhanced both Free Dox and Doxil treatment (Fig. 4d). It should be kept in mind that 4T1 triple-negative breast cancer is an aggressively growing model, which is not very amenable to immunomodulatory therapy. It is therefore unlikely that complete cures can be achieved in this model using the therapeutic protocol employed here. Systemic toxicity was not increased upon adding CCL2i treatment to chemotherapy, as evidenced by similar body weight development over time (Fig. S1a-c).

We also analyzed the composition of the tumor microenvironment upon CCL2 inhibition. This was done for the group with the best efficacy (Doxil and Doxil + CCL2i), in comparison to the control group. Using H&E staining and IHC, we determined the percentages of cancer cells, stroma cells, lymphocytes and blood vessels. Images of entire tumors and of selected regions of interest were acquired, and the respective cell types were identified (Fig. 4e-l). Tumor-infiltrating lymphocytes (TIL), epithelioid-like cancer cells, spindle-like stromal cells and vessels were differentiated on the basis of their nuclear morphology (Fig. 4i-l). It was found that upon CCL2i treatment, the area fractions of cancer cells and stromal cells were reduced, while the fraction of TIL was increased (Fig. 4m-n).

We next analyzed the levels T and Natural Killer (NK) lymphocytes in tumors and in blood upon CCL2 inhibition. This was done using flow cytometry (Fig. 5). Quantification of $CD8^+$ T cells in tumor tissue, identified via $TCR\beta^+$ and $CD8a^+$ double-staining, showed a >3-fold increase in infiltration of cytotoxic T cells in CCL2i treated tumors as compared to control tumors (Fig. 5a-c). Upon combining CCL2i with Doxil, an almost 2-fold increase in cytotoxic T cells was found, but this difference was of borderline (in)significance ($p = 0.05$; Fig. 5d-f). In line with these observations, the levels of $CD8^+$ T cells in blood were also found to be increased upon CCL2i treatment, both for control vs. CCL2i (Fig. 52 m-o), and for Doxil vs. Doxil + CCL2i (Fig. 5p-r). We furthermore quantified the levels of $CD4^+$ T helper cells, of γδ T cells (which play a prominent role in cytokine release), and of NK (natural killer) cells, both in tumors (Fig. 5g-l) and in circulation (Fig. 5s-x). In almost all cases, increases in T lymphocyte populations were observed upon CCL2 inhibition. These differences were sometimes statistically significant, sometimes not, and they did not linearly correlate with the observed therapeutic responses. This is likely due to biological variability in systemic responses to (combination) therapy, as well as to the relatively small sample number ($n = 3$ tumors were used for flow cytometry). We finally also used flow cytometry to assess the levels of M1-like ($MHCII^{high}$) and M2-like ($MHCII^{low}$) TAM in tumors upon CCL2i monotherapy and CCL2i + Doxil combination therapy. In the line with the results presented in Fig. 2n-o, we observed a stronger reduction in M2-like TAM than in M1-like TAM upon CCL2 inhibition (Fig. S2a,c). Treatment with Doxil potentiated these effects, showing overall much lower levels of TAM in tumors, as well as a much stronger reduction in M2-like TAM (Fig. S2b,d). Altogether, these findings illustrate that CCL2i can beneficially affect the tumor and blood levels of lymphoid and myeloid cell populations.

Normalized blood vessels have been previously shown to be able to contribute to improved T cell infiltration in tumors, which results in a positive feedback loop that supports more M1-like myeloid cells, to create an increasingly pro-immunogenic tumor microenvironment [45]. Retrospective and prospective studies have furthermore convincingly shown that T cell presence in tumors is a predictive biomarker for better response to and survival upon checkpoint inhibition-based immunotherapy and (nano)chemotherapy, in different tumor entities including triple-negative breast cancer [46–51].

In summary, our results demonstrate that inhibition of CCR2-positive macrophage infiltration in tumors using the anti-CCL2 L-RNA aptamer mNOX-E36 attenuates tumor growth and pathological angiogenesis in orthotopic 4T1 triple-negative breast cancer tumors in mice. Additional experiments in other tumor models are needed to corroborate these findings. Our work adds to the growing pool of experimental evidence identifying TAM modulation as an appealing pharmacological strategy to enhance anti-tumor therapy. For example, depleting TAM with clodronate-encapsulated liposomes potently reduced tumor growth in various different cancer types [52]. Reducing the levels of CSF-1 with siRNA or antibodies resulted in TAM depletion and inhibited neuroblastoma tumor growth and angiogenesis [53]. We observed that attenuating TAM infiltration resulted in enhanced vessel maturation and functionality, which indicates that anti-CCL2 treatment leads to vascular normalization. Anti-CCL2 tumor priming enhanced the delivery of polymers and liposomes, and potentiated the efficacy of doxorubicin and Doxil. These effects are in line with previous papers demonstrating the added value of vascular normalization and priming on the accumulation and efficacy of drugs and drug delivery systems [25,44,54–56]. Together, our findings imply that pharmacological inhibition of macrophage infiltration and the resulting priming of tumor blood vessels is an interesting strategy for improving tumor-directed drug delivery and combined modality anticancer therapy.

4. Conclusion

Blocking CCL2-dependent macrophage infiltration in tumors using the L-RNA aptamer mNOX-E36 inhibits pathological angiogenesis. Anti-CCL2 treatment induces features of vascular normalization and improves tumor perfusion, thereby enhancing tumor-targeted drug delivery and anticancer nanotherapy. These findings exemplify the potential of pharmacological priming tumors for improved delivery and efficacy of drugs and drug delivery systems.

Author contributions

Twan Lammers conceived the study. Diana Möckel, Josef Ehling and Twan Lammers were responsible for the study concept and experimental design. Fabian Kiessling, Frank Tacke and Twan Lammers supervised the work. Marek Weiler, Robert Pola, Michal Pechar, Tomas Etrych and Gert Storm produced and characterized nanomedicine formulations. Dirk Eulberg contributed the CCL2-inhibiting L-RNA aptamer mNOX-E36. Diana Möckel performed in vivo experiments. Diana Möckel, Maike Baues and Elena Rama performed immunohistological stainings and image acquisition. Diana Möckel, Matthias Bartneck, Patricia Niemietz analyzed the gene expression data. Felix Gremse provided the Imalytics Preclinical software and incorporated new features for the analysis of the in vivo data specifically for this study. Diana Möckel and Matthias Bartneck produced the figures. Diana Möckel drafted the manuscript. All authors read, revised, and approved the manuscript.

Funding

The authors acknowledge financial support by the European Research Council (ERC-CoG: Meta-Targeting 864121), the German Research Foundation (DFG: GRK2375 (grant number 331065168), LA-2937/4–1, SFB1066 and BA622/2–1), the Wilhelm Sander Foundation (2018.129.1) and the Ministry of Health of the Czech Republic (NU21–08-00280). Active support by the Two-Photon Imaging Core Facility at the Interdisciplinary Center for Clinical Research (IZKF) at the Faculty of Medicine at RWTH Aachen University is also gratefully acknowledged.

CRediT authorship contribution statement

Diana Möckel: Conceptualization, Data curation, Formal analysis, Investigation, Methodology, Writing – original draft, Visualization. **Matthias Bartneck:** Data curation, Formal analysis, Methodology. **Patricia Niemietz:** Data curation, Investigation. **Maike Wagner:** Investigation, Methodology. **Josef Ehling:** Conceptualization, Methodology. **Elena Rama:** Data curation, Formal analysis, Investigation. **Marek Weiler:** Methodology. **Felix Gremse:** Methodology, Software. **Dirk Eulberg:** Resources. **Robert Pola:** Resources. **Michal Pechar:** Resources. **Tomas Etrych:** Resources. **Gert Storm:** Writing – review & editing. **Fabian Kiessling:** Resources, Writing – review & editing. **Frank Tacke:** Conceptualization, Funding acquisition, Methodology, Supervision, Writing – review & editing. **Twan Lammers:** Conceptualization, Funding acquisition, Methodology, Resources, Supervision, Validation, Visualization, Writing – review & editing.

Declaration of Competing Interest

Dirk Eulberg is an employee of TME Pharma AG. Felix Gremse is the owner of Gremse-IT, licensing the image analysis software IMALYTICS Preclinical. None of the other authors has any relevant conflict of interest.

Data availability

Data will be made available on request.

Appendix A. Supplementary data

Supplementary data to this article can be found online at https://doi.org/10.1016/j.jconrel.2023.11.044.

References

[1] E. Bridges, A.L. Harris, Vascular-promoting therapy reduced tumor growth and progression by improving chemotherapy efficacy, Cancer Cell 27 (1) (2015) 123–137.
[2] J.K. Saggar, M. Yu, Q. Tan, I.F. Tannock, The tumor microenvironment and strategies to improve drug distribution, Front. Oncol. 3 (2013) 154.
[3] L.Y. Rizzo, B. Theek, G. Storm, F. Kiessling, T. Lammers, Recent progress in nanomedicine: therapeutic, diagnostic and theranostic applications, Curr. Opin. Biotechnol. 24 (6) (2013) 1159–1166.
[4] T. Lammers, F. Kiessling, W.E. Hennink, G. Storm, Drug targeting to tumors: principles, pitfalls and (pre-) clinical progress, J. Control. Release 161 (2012) 175–187.
[5] J. Wu, The enhanced permeability and retention (EPR) effect: the significance of the concept and methods to enhance its application, J. Pers. Med. 11 (8) (2021 Aug 6) 771.
[6] S.K. Golombek, J.N. May, B. Theek, et al., Tumor targeting via EPR: strategies to enhance patient responses, Adv. Drug Deliv. Rev. 130 (2018 May) 17–38.
[7] H. Maeda, H. Nakamura, J. Fang, The EPR effect for macromolecular drug delivery to solid tumors: improvement of tumor uptake, lowering of systemic toxicity, and distinct tumor imaging in vivo, Adv. Drug Deliv. Rev. 65 (1) (2013 Jan) 71–79.
[8] R.K. Jain, Antiangiogenesis strategies revisited: from starving tumors to alleviating hypoxia, Cancer Cell 26 (5) (2014) 605–622.
[9] T.T. Batchelor, E.R. Gerstner, K.E. Emblem, et al., Improved tumor oxygenation and survival in glioblastoma patients who show increased blood perfusion after cediranib and chemoradiation, PNAS. 110 (47) (2013) 19059–19064.
[10] S. Goel, D.G. Duda, L. Xu, et al., Normalization of the vasculature for treatment of cancer and other diseases, Physiol. Rev. 91 (3) (2011) 1071–1121. . Jul.
[11] R.K. Jain, Normalizing tumor vasculature with anti-angiogenic therapy: a new paradigm for combination therapy, Nat. Med. 7 (9) (2001 Sep) 987–989.
[12] C. Murdoch, A. Giannoudis, C.E. Lewis, Mechanisms regulating the recruitment of macrophages into hypoxic areas of tumors and other ischemic tissues, Blood. 104 (8) (2004 Oct 15) 2224–2234.
[13] L. Bingle, N.J. Brown, C.E. Lewis, et al., J. Pathol. 196 (3) (2002 Mar) 254–265.
[14] J. Ehling, M. Bartneck, X. Wei, et al., CCL2-dependent infiltrating macrophages promote angiogenesis in progressive liver fibrosis, Gut 63 (12) (2014 Dec) 1960–1971.
[15] C. Murdoch, M. Muthana, S.B. Coffelt, C.E. Lewis, The role of myeloid cells in the promotion of tumuor angiogenesis, Nat. Rev. Cancer 8 (8) (2008 Aug) 618–631.
[16] M. Craig, R.D. Loberg, CCL2 (monocyte chemoattractant protein-1) in cancer bone metastases, Cancer Metastasis Rev. 25 (4) (2006 Dec) 611–619.
[17] M. Bartneck, P.L. Schrammen, D. Möckel, et al., The CCR2^{+} macrophages subset promotes pathogenic angiogenesis for tumor vascularization in fibrotic livers, Cell. Mol. Gastroenterol. Hepatol. 7 (2) (2019) 371–390.
[18] P. Chen, P. Bonaldo, Role of macrophage polarization in tumor angiogenesis and vessel normalization: implications for new anticancer therapies, Int. Rev. Cell Mol. Biol. 301 (2013) 1–35.
[19] B.-Z. Qian, J. Li, H. Zhang, et al., CCL2 recruits inflammatory monocytes to facilitate breast-tumour metastasis, Nature 475 (7355) (2011 Jun 8) 222–225.
[20] Clinical Trial, A Phase IIa Study to Characterize the effects of CCL2 Inhibition with the Spiegelmer NOX-E36 in Patients with Type 2 Diabetes Mellitus and Albuminuria, 2012. NCT01547897.
[21] A. Vater, S. Klussmann, Turning mirror-image oligonucleotides into drugs: the evolution of Spiegelmer therapeutics, Drug Discov. Today 20 (1) (2015) 147–155.
[22] P. Chowdhury, U. Ghosh, K. Samanta, et al., Bioactive nanotherapeutic trends to combat triple negative breast cancer, Bioact. Mater. 6 (10) (2021) 3269–3287.
[23] Bianchini Giampaolo, J.M. Balko, I.A. Mayer, M.E. Sanders, L. Gianni, Triple-negative breast cancer: challenges and opportunities of a heterogeneous disease, Nat. Rev. Clin. Oncol. 13 (11) (2016 Nov) 674–690.
[24] T. Opacic, S. Dencks, B. Theek, et al., Motion model ultrasound localization microscopy for preclinical and clinical multiparametric tumor characterization, Nat. Commun. 9 (1) (2018 Apr 18) 1527.
[25] B. Theek, M. Baues, F. Gremse, et al., Histidine-rich glycoprotein-induced vascular normalization improves EPR-mediated drug targeting to and into tumors, J. Control. Release 282 (2018 Jul 28) 25–34.
[26] B. Theek, M. Baues, T. Ojha, et al., Sonoporation enhances liposome accumulation and penetration in tumors with low EPR, J. Control. Release 231 (2016 Jun 10) 77–85.
[27] J.N. May, S.K. Golombek, M. Baues, et al., Multimodal and multiscale optical imaging of nanomedicine delivery across the blood-brain barrier upon sonopermeation, Theranostics 10 (4) (2020 Jan 12) 1948–1959.
[28] H. Zhang, Thin-film hydration followed by extrusion method for liposome preparation, Methods Mol. Biol. 1522 (2017) 17–22.
[29] F. Gremse, M. Stärk, J. Ehling, et al., Imalytics preclinical: interactive analysis of biomedical volume data, Theranostics 6 (3) (2016 Jan 1) 328–341.
[30] F. Gremse, D. Doleschel, S. Zafarnia, et al., Hybrid μCT-FMT imaging and image analysis, J. Vis. Exp. 100 (2015) e52770.
[31] F. Gremse, B. Theek, S. Kunjachan, et al., Absorption reconstruction improves biodistribution assessment of fluorescent nanoprobes using hybrid fluorescence-mediated tomography, Theranostics. 4 (10) (2014) 960–971.
[32] S. Kunjachan, F. Gremse, B. Theek, et al., Noninvasive optical imaging of nanomedicine biodistribution, ACS Nano 7 (1) (2013) 252–262.
[33] J. Ehling, B. Theek, F. Gremse, et al., Micro-CT imaging of tumor angiogenesis: quantitative measures describing micromorphology and vascularization, Am. J. Pathol. 184 (2) (2014 Feb) 431–441.
[34] Z. Wu, A. Curaj, S. Fokong, et al., Rhodamine-loaded intercellular adhesion molecule–1-targeted microbubbles for dual-modality imaging under controlled shear stresses, Circ. Cardiovasc. Imaging 6 (2013) 974–981.
[35] A. Sica, P. Larghi, A. Mancino, et al., Macrophage polarization in tumour progression, Semin. Cancer Biol. 18 (5) (2008 Oct) 349–355.
[36] H. Cheng, Z. Wang, L. Fu, T. Xu, Macrophage polarization in the development and progression of ovarian cancers: an overview, Front. Oncol. 9 (2019) 421.
[37] J. Liu, X. Geng, J. Hou, G. Wu, New insights into M1/M2 macrophages: key modulators in cancer progression, Cancer Cell Int. 21 (1) (2021 Jul 21) 389.
[38] K. Movahedi, D. Laoui, C. Gysemans, et al., Different tumor microenvironments contain functionally distinct subsets of macrophages derived from Ly6C(high) monocytes, Cancer Res. 70 (14) (2010 Jul 15) 5728–5739.
[39] V. Riabov, A. Gudima, N. Wang, et al., Role of tumor associated macrophages in tumor angiogenesis and lymphangiogenesis, Front. Physiol. 5 (5) (2014) 75.
[40] L. Bai, Z. Hu, T. Han, et al., Super-stable cyanine@albumin fluorophore for enhanced NIR-II bioimaging, Theranostics. 12 (10) (2022 May 26) 4536–4547.
[41] E. Zheng, S. Luo, X. Tan, C. Shi, Mechanistic study of IR-780 dye as a potential tumor targeting and drug delivery agent, Biomaterials. 35 (2) (2014 Jan) 771–778.
[42] V.P. Chauhan, T. Stylianopoulos, Y. Boucher, R.K. Jain, Delivery of molecular and nanoscale medicine to tumors: transport barriers and strategies, Annu. Rev. Chem. Biomol. Eng. 2 (2011) 281–298.
[43] Y. Huang, S. Goel, D.G. Duda, D. Fukumura, R.K. Jain, Vascular normalization as an emerging strategy to enhance cancer immunotherapy, Cancer Res. 73 (10) (2013 May 15) 2943–2948.
[44] V.P. Chauhan, T. Stylianopoulos, J.D. Martin, Z. Popovic, et al., Normalization of tumour blood vessels improves the delivery of nanomedicines in a size-dependent manner, Nat. Nanotechnol. 7 (6) (2012 Apr 8) 383–388.
[45] M. Ghosh, A.M. Lenkiewicz, B. Kaminska, The interplay of tumor vessels and immune cells affects immunotherapy of glioblastoma, Biomedicines. 10 (9) (2022 Sep 15) 2292.
[46] J. Galon, D. Bruni, Approaches to treat immune hot, altered and cold tumours with combination immunotherapies, Nat. Rev. Drug Discov. 18 (3) (2019 Mar) 197–218.
[47] J. Galon, D. Bruni, Tumor immunology and tumor evolution: intertwined histories, Immunity. 52 (1) (2020 Jan 14) 55–81.
[48] I.B. Heppner, M. Untch, C. Denkert, et al., Tumor-infiltrating lymphocytes: a predictive and prognostic biomarker in neoadjuvant-treated HER2-positive breast cancer, Clin. Cancer Res. 22 (2016) 5747–5754.
[49] S. Dushyanthen, P.A. Beavis, P. Savas, et al., Relevance of tumor-infiltrating lymphocytes in breast cancer, BMC Med. 13 (2015) 202.

[50] M.M. Tu, H.A. Abdel-Hafiz, R.T. Jones, et al., Inhibition of the CCL2 receptor, CCR2, enhances tumor response to immune checkpoint therapy, Commun. Biol. 3 (1) (2020 Nov 27) 720.
[51] L. Barrueto, F. Caminero, L. Cash, et al., Resistance to checkpoint inhibition in cancer immunotherapy, Transl. Oncol. 13 (3) (2020 Mar), 100738.
[52] B.-Z. Qian, J.W. Pollard, Macrophage diversity enhances tumor progression and metastasis, Cell 141 (1) (2010 Apr 2) 39–51.
[53] D. Abraham, K. Zins, M. Sioud, et al., Stromal cell-derived CSF-1 blockade prolongs xenograft survival of CSF-1-negative neuroblastoma, Int. J. Cancer 126 (6) (2010 Mar 15) 1339–1352.
[54] T. Stylianopoulos, R.K. Jain, Combining two strategies to improve perfusion and drug delivery in solid tumors 110 (46) (2013 Oct) 18632–18637.
[55] T. Stylianopoulos, L.L. Munn, R.K. Jain, Reengineering the physical microenvironment of tumors to improve drug delivery and efficacy: from mathematical modeling to bench to bedside 4 (4) (2018 Apr) 292–319.
[56] D. Doleschel, A. Rix, S. Arns, et al., Erythropoietin improves the accumulation and therapeutic effects of carboplatin by enhancing tumor vascularization and perfusion, Theranostics. 5 (8) (2015 May 1) 905–918.